PAPER • OPEN ACCESS

Reduced recombination through CZTS/CdS interface engineering in monograin layer solar cells

To cite this article: M Kauk-Kuusik *et al* 2022 *J. Phys. Energy* **4** 024007

View the article online for updates and enhancements.

Journal of Physics: Energy

PAPER

Reduced recombination through CZTS/CdS interface engineering in monograin layer solar cells

M Kauk-Kuusik[1,*] , K Timmo[1] , K Muska[1] , M Pilvet[1] , J Krustok[1] , M Danilson[1] , V Mikli[1] ,
R Josepson[2] and M Grossberg-Kuusk[1]

1   Department of Materials and Environmental Technology, Tallinn University of Technology, Ehitajate tee 5, 19086 Tallinn, Estonia
2   Division of Physics, Tallinn University of Technology, Ehitajate tee 5, 19086 Tallinn, Estonia
*   Author to whom any correspondence should be addressed.

E-mail: marit.kauk-kuusik@taltech.ee

Abstract

The power conversion efficiency of Cu_2ZnSnS_4 (CZTS) solar cells is still limited by deep defects, low minority carrier lifetime and high recombination rates at the CZTS/CdS interface. The objective of this study was to find an effective method to reduce interface recombination of CZTS monograin layer solar cells. A two-step heterojunction formation process was applied by controlling the intermixing of Cd and Cu in the CZTS/CdS interface, which resulted in improved device efficiency of up to 11.7%. Surface analysis by x-ray photoelectron spectroscopy confirmed Cd diffusion into the surface of CZTS after CdS air-annealing by forming an ultra-thin $Cu_2Zn_xCd_{1-x}SnS_4$ layer. Moreover, external quantum efficiency measurements showed that the absorption edge shifts to longer wavelengths with the addition of Cd into the CZTS surface layer. This surface modification and replacement of a CdS:Cu buffer layer by fresh CdS greatly reduced the interface recombination and improved the junction quality, contributing to an enhancement of $J_{SC} \sim 3$ mA cm^{-2} (from 20.5 to 23.6 mA cm^{-2}) and fill factor $\sim 14\%$ (from 59.4% to 67.7%). The serial resistance of the CZTS monograin layer solar cells was significantly reduced from 2.4 Ω cm^2 to 0.67 Ω cm^2. To understand the electrical behavior of the highest-efficiency CZTS monograin layer solar cell in more detail, the temperature-dependent current–voltage characteristics were analyzed.

1. Introduction

Photovoltaic technology can provide a significant fraction of the world's energy demands if solar devices are composed of Earth-abundant and nontoxic materials. Among the inorganic absorber materials, kesterite materials $(Cu_2ZnSn(S,Se)_4)$ are promising candidates because they combine near optimum direct band gap, a high optical absorption coefficient of $\sim 10^4$ cm^{-1} in the visible light region, predicted theoretical power conversion efficiency (PCE) of more than 30%, and constituent elements that are Earth-abundant, cheap, and nontoxic. The major issue for kesterite is a low open circuit voltage (V_{OC}) due to low minority carrier lifetime [1] and high recombination rates at the heterojunction interface as well as in the bulk. The highest recorded efficiency for a Cu_2ZnSnS_4 (CZTS)-based solar cell has been reported to be 11% [2]. The highest V_{OC} of 809 mV is demonstrated for ordered CZTS [3]. Regardless of these achievements, the V_{OC} deficit is still large compared to $Cu(In,Ga)Se_2$ (CIGS)-based solar cells and, therefore, significant research is still needed in this field. Several groups have shown improvements in PCE with elemental intermixing at the absorber/buffer interface by post-annealing process [2, 4]. Su *et al* [5] reported that by post-annealing a complete Cd-alloyed pure sulfide device, which included ITO as a window layer, showed efficiency of 12.6%. Our group's latest study [6] showed that soft air-annealing of CZTS/CdS at 175 °C–200 °C improved device performance mainly due to decreased series resistance (R_S), but annealing at higher temperature degraded the devices due to the formation of a Cu-rich CZTS absorber surface close to the CZTS/CdS interface. Analysis results showed that our CZTS monograin layer solar cells have several recombination routes.

Unfortunately, none of these routes disappeared with air annealing of the CZTS/CdS interface. Therefore, the post-annealing of CZTS/CdS is not a definite solution for reducing interface recombination and solving the V_{OC} deficit. It must also be considered that with post-annealing of CZTS/CdS, diffusion of Cu from the absorber to the buffer layer is possible, which increases the photoconductivity of CdS and increases the R_S of devices [7, 8]. Another option to reduce recombination and boost V_{OC} is a Cd ion soaking treatment, which is also used in CIGS technologies [9–11]. Results have shown that the Cd ion soaking process facilitates Cd diffusion into the CZTS surface [10, 12], increases the minority carrier lifetime and reduces the non-radiative recombination [10], and decreases the R_S of the CZTS devices [9].

An enhancement in the performance of CZTS monograin layer solar cells has been achieved in several ways. For example, the addition of a low concentration of Ag (1% from Cu) into $Cu_2(Cd,Zn)SnS_4$ lattice led to increased V_{OC} values of the devices and improved the efficiency from 6.6% to 8.7% due to the reduction in non-radiative recombination and/or interface recombination, but the V_{OC} deficit remained unsolved [13]. The influence of order–disorder in CZTS monograin powders was investigated in the study [14]. The results showed that the low-temperature thermal treatments increased the degree of Cu–Zn ordering and devices showed increased V_{OC} values up to 784 mV and CZTS monograin layer solar cell efficiency of 9.1%. Nevertheless, the V_{OC} deficit still remained large compared to corresponding band gap values (E_g). A photoluminescence (PL) study showed that reduced Cu–Zn disordering of the crystals led to increased band gap energy by about 100 meV and a change in recombination type from band to tail to band to impurity type. The latter involves deep trap ($\sim$200 meV) related recombination and reduces the positive effect of the band gap increase to the V_{OC} in the least disordered material. Moreover, the performance of CZTS monograin layer solar cells was effectively improved up to 9.4% by using oxidative chemical treatment before the formation of the heterojunction [15]. The effect was attributed to the formation of a passivation layer of SnO_2 on the CZTS surface. Although all our previous developments have shown good progress, the main issues have remained.

In this study, we applied a two-step process in the heterojunction formation to reduce the interface recombination and improve the junction quality, and the current–voltage (*I–V*) measurements showed device efficiency of up to 11.7%. The serial resistance of the CZTS monograin layer solar cells was significantly reduced from 2.4 Ω cm^2 [6] to 0.67 Ω cm^2. In this work, we analyze the influence of Cd diffusion into the surface of CZTS and replacement of Cu-doped CdS by a fresh CdS buffer layer on the electrical behavior of the highest-efficiency CZTS monograin layer solar cell by temperature-dependent *I–V* characteristics.

2. Experimental

In this work, Cu_2ZnSnS_4 monograin powder was synthesized from binary compounds CuS, ZnS and SnS with purity of 99.999% in the liquid phase of potassium iodide (KI) flux material in a sealed quartz ampoule at 740 °C. The composition of the monograins was analyzed by energy dispersive x-ray spectroscopy. The bulk of the crystals had average composition ratios of Cu/(Zn +Sn) = 0.91 and Zn/Sn = 1.08. The standard post-growth processes in use in our laboratory were applied. Post-growth chemical etching was done with 1 vol% Br in methanol for 5 min followed by 10 wt% Potassium cyanide (KCN) aqueous solution for 5 min at room temperature. After the etching process, the CZTS powder was heat-treated in a sealed ampoule in a dual temperature zone furnace at 840 °C in S vapor (p_S = 2050 Torr) for 60 min.

The highest-efficiency CZTS monograin layer solar cell (hereafter named as CZTS-modified) was prepared by using a two-step process (scheme of the combined two-step process in figure 1) for formation of heterojunction between the CZTS and CdS. In the first step, CdS was deposited by a chemical bath deposition process on powder crystals followed by annealing in air at 225 °C for 10 min [6]. With this step, Cd diffusion into the surface of CZTS, forming an ultra-thin $Cu_2Zn_xCd_{1-x}SnS_4$ layer with a decreased band gap at the very top of the absorber, is expected. At the same time, Cu out-diffusion into the surface of the CZTS and also into the buffer layer is possible and this could change the properties of the buffer layer. Therefore, after the annealing step, CdS was removed by concentrated HCl. As a second step, a fresh CdS buffer layer without additional post-annealing was deposited on the CZTS crystals. A CZTS monograin layer solar cell with single-step CdS buffer layer deposition was considered as a reference device in this study (hereafter named CZTS-ref). Subsequently, CdS-covered crystals were implemented in the so-called monograin membranes. The membranes consist of a thin layer of transparent, low-shrinkage polymer into which microcrystals are semi-immersed in the middle of the curing process. The front side of the crystals remains intact from the polymer and, after complete polymerization, the membranes are covered with a window layer. More details about preparation of the monograin layer solar cells are described in [6].

Scanning electron microscopy (SEM) and electron beam induced current (EBIC) measurements were performed using a Merlin, Carl Zeiss Microscopy, Germany. EBIC mapping was performed by a specimen
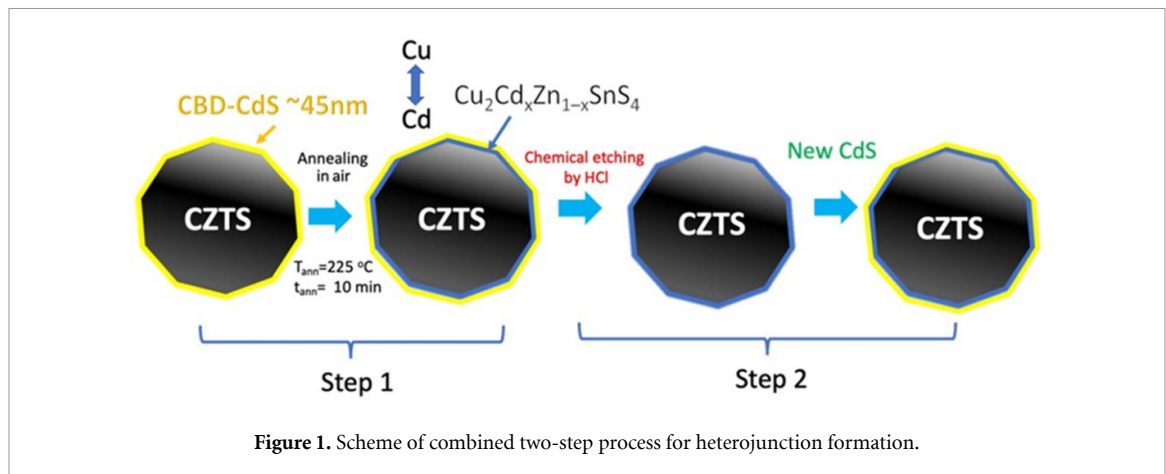
Figure 1. Scheme of combined two-step process for heterojunction formation.

current amplifier, model—Type 31, GW Electronics Inc., USA. Accelerating voltages of 20 kV for surface EBIC mapping and 10 kV for cross-section imaging were used in the SEM.

The room temperature current–voltage characteristics of monograin layer solar cells were measured with a Keithley 2400 source meter under standard test conditions (AM 1.5, 100 mW cm^{-2}) using a Newport Oriel Class A 91195A solar simulator. The temperature-dependent measurements were performed in a closed-cycle He cryostat (Janis CCS-150) using a halogen lamp. The position of the halogen lamp was calibrated to match the current value measured standard test conditions. The external quantum efficiency (EQE) was measured using a computer-controlled SPM-2 prism monochromator. The generated photocurrent was detected at 0 V bias voltage at room temperature by using a 250 W halogen lamp and DSP lock-in amplifier.

Compositional changes at the CTS interface were analyzed by a Kratos Analytical AXIS Ultra DLD x-ray photoelectron spectrometer (XPS). In order to collect the signal of photoexcited electrons, CZTS powder mounted on a rotational sample holder by ultra-high vacuum proof carbon tape was excited by a monochromatic Al Kα x-ray source (1486.6 eV) at 15 kV and 150 W. Hybrid lens mode in conjunction with an aperture slot view (700×300 μm) and pass energies of 160 eV and 20 eV were set to collect the survey and high-resolution photoelectron spectra, respectively. After subtraction of the Shirley background, high-resolution experimental peaks were deconvoluted with Voigt functions and a nonlinear squares fitting algorithm in order to determine core-level peak positions.
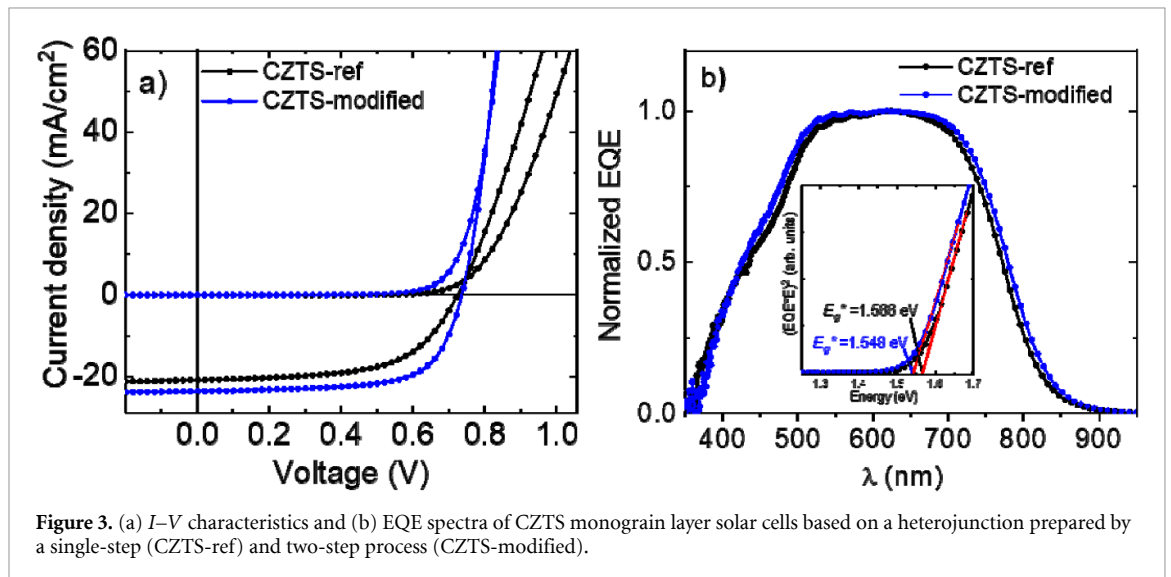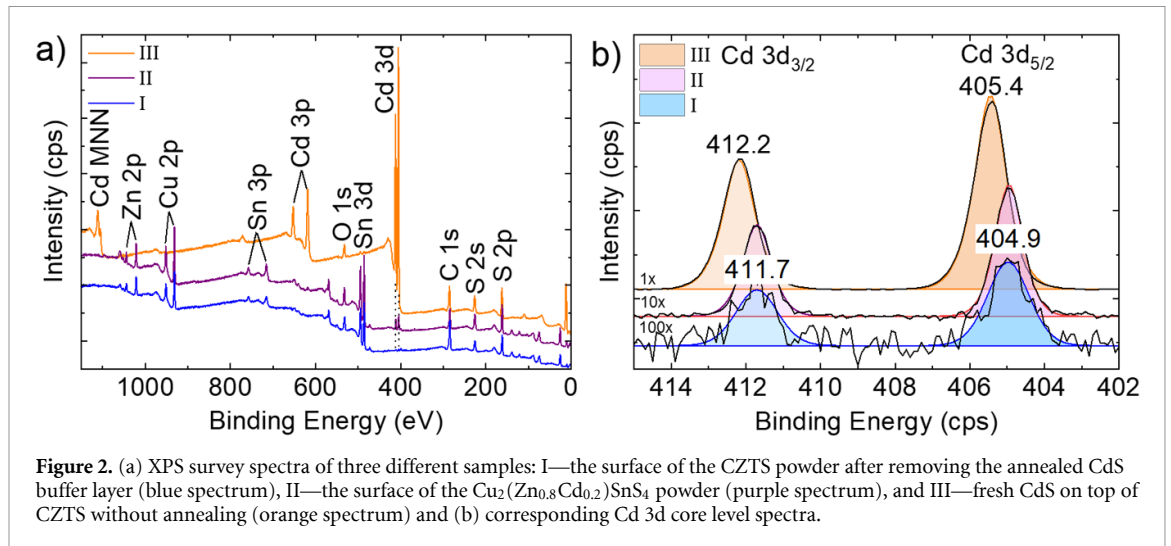
3. Results and discussion

3.1. XPS analysis

The surface composition of the CZTS powder after the first CdS deposition process followed by air–annealing at 225 °C was investigated by XPS. Figure 2(a) shows the XPS survey spectrum of three different samples: I—the surface of the CZTS powder after removing the annealed CdS buffer layer (blue spectrum), II—the surface of the $Cu_2(Zn_{0.8}Cd_{0.2})SnS_4$ powder as a proof of Cd inclusion in the lattice (purple spectrum), and III—fresh CdS on top of CZTS without annealing (orange spectrum). $Cu_2(Zn_{0.8}Cd_{0.2})SnS_4$ powder was also investigated in the previous study [13]. Figure 2(b) shows the high-resolution spectra of the Cd 3d core level. The peaks of Cd 3d$_{3/2}$ and Cd 3d$_{5/2}$, which are located at 412.2 and 405.4 eV, can be assigned to Cd^{2+} in CdS. The Cd 3d peaks at 411.7 and 404.9 eV correspond to Cd^{2+} in $Cu_2(Zn_xCd_{1-x})SnS_4$ solid solution. The latter peak positions for Cd^{2+} in solid solution are in good agreement with literature reports [16, 17]. This gives us a solid proof that after CZTS/CdS air-annealing an ultra-thin $Cu_2Zn_xCd_{1-x}SnS_4$ layer on CZTS crystals was formed. The signal of O 1s and C 1s in every survey spectrum is due to atmospheric contamination.

3.2. Device characterization

The room temperature *I–V* characteristics and EQE of the studied CZTS monograin layer solar cells are shown in figures 3(a) and (b), respectively. The black curves in both figures belong to the monograin layer solar cell based on CZTS covered by a non-annealed CdS buffer layer as a reference device in this study (CZTS-ref). The blue curves belong to the CZTS monograin layer solar cell prepared by using a two-step process for formation of a heterojunction between the CZTS and CdS (CZTS-modified). The combined process for heterojunction formation slightly improved V_{OC} values from 723 mV to 735 mV, the main improvement was in the current density values (J_{SC}) from 20.5 to 23.6 mA cm^{-2}, and in fill factor (FF) from 59.4% to 67.7%. The serial resistance of the monograin layer solar cells based on the CZTS-modified absorber was significantly reduced from 2.4 Ω cm^2 to 0.67 Ω cm^2. As a result, enhanced device performance

Figure 2. (a) XPS survey spectra of three different samples: I—the surface of the CZTS powder after removing the annealed CdS buffer layer (blue spectrum), II—the surface of the $Cu_2(Zn_{0.8}Cd_{0.2})SnS_4$ powder (purple spectrum), and III—fresh CdS on top of CZTS without annealing (orange spectrum) and (b) corresponding Cd 3d core level spectra.

Figure 3. (a) *I–V* characteristics and (b) EQE spectra of CZTS monograin layer solar cells based on a heterojunction prepared by a single-step (CZTS-ref) and two-step process (CZTS-modified).

with PCE of 11.7% was obtained. PCE is calculated by using an image analysis tool for the active surface area (yellow area ∼75% of total contact area), which is estimated from the EBIC top view image (figure 4(a)).

EBIC allows imaging of the collection efficiency of charge carriers in the device. In EBIC, the electron beam illuminates a nanometer-scale region in the semiconductor specimen and generates electron–hole pairs. A portion of them are collected at the device contacts, giving rise to a photocurrent. By scanning the electron beam, a two-dimensional map of collected photocurrent in the device is constructed [18]. Figure 4(b) shows a higher-magnification EBIC top view of the monograin layer solar cell. The dark areas are non-conductive polymer, where charge-carriers are not generated and light areas show working crystals, where photocurrent is produced. The EBIC cross-section image in figure 4(c) is shown as a split picture of secondary electron and photocurrent images obtained simultaneously, showing on one side the SEM and on the other side the EBIC image.

The EQE spectrum was used to study the spectral response of the CZTS monograin layer solar cells. Figure 3(b) shows the normalized EQE spectra of monograin layer solar cells based on the CZTS-ref and CZTS-modified heterojunction. The absorption edge shifts to longer wavelengths with addition of Cd into the CZTS surface layer. The effective band gap energy (E_g^*) of the absorber material was evaluated from the linear segment of the low-energy side of the construction $(EQE*E)^2$ vs. *E* curves. A slight decrease of E_g^* from 1.566 eV to 1.548 eV was found, which might be due to the formation of an ultra-thin $Cu_2Zn_xCd_{1-x}SnS_4$ layer on the CZTS crystals [2].

To understand in more detail the electrical behavior of the highest-efficiency CZTS monograin layer solar cell, the temperature-dependent current–voltage characteristics were analyzed.
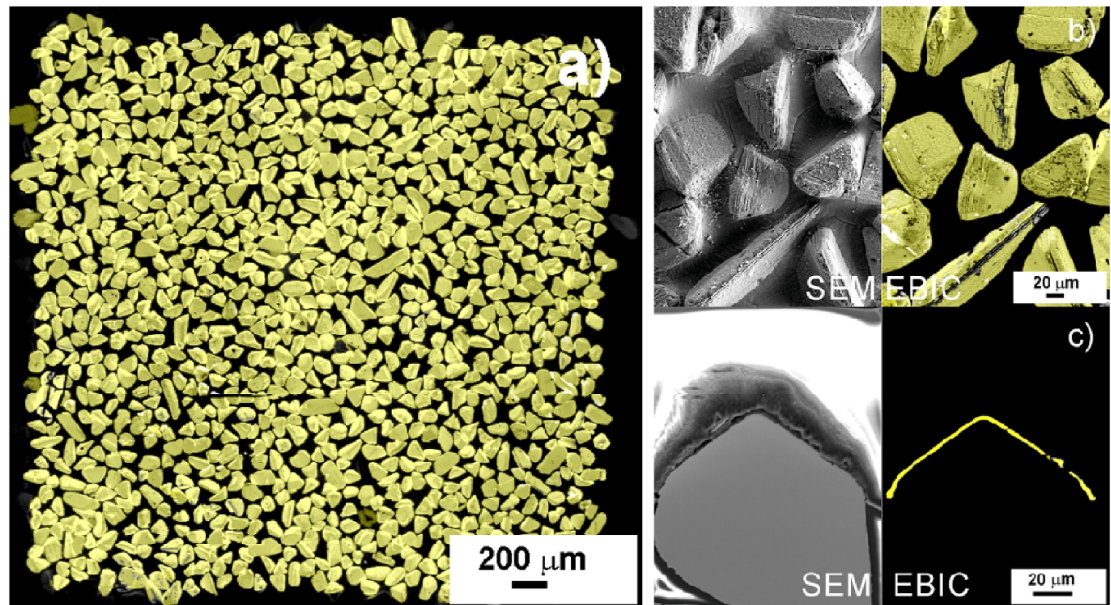
Figure 4. Photocurrent image of (a) full device with size 3.1×3.1 mm^2, (b) SEM and EBIC images from top view of the same area of the device, and (c) SEM and EBIC image from cross-section of the same area of the device.
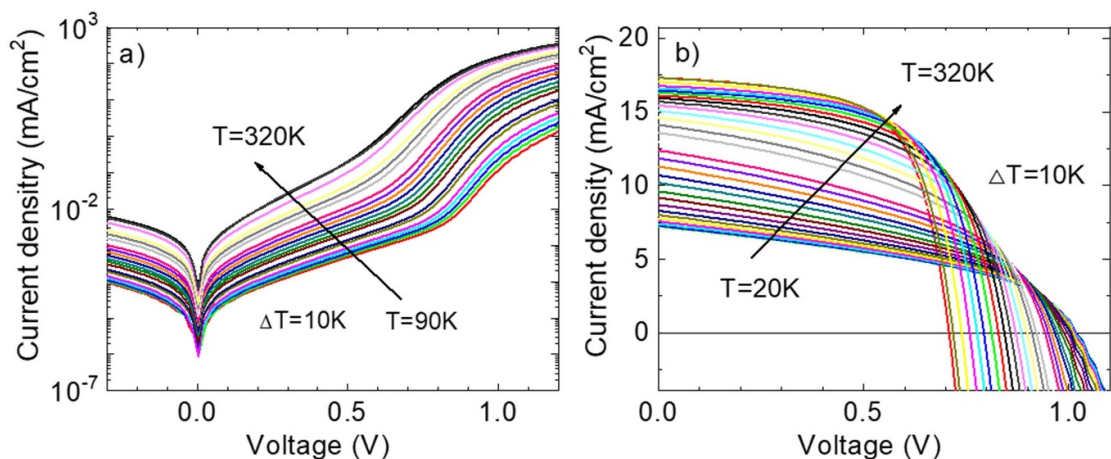
Figure 5. Temperature dependence of (a) dark and (b) illuminated *I–V* curves of CZTS-modified device.

3.3. Temperature dependence of *I–V* characteristics

The dark and illuminated *I–V* curves of the CZTS-modified device measured at different temperatures are presented in figures 5(a) and (b). The solar cell parameters obtained from direct measurements are presented in figures 6(a) and (b). The maximum efficiency was achieved at $T = 270$ K mostly due to higher FF and V_{OC}. The calculated efficiencies are not calibrated because we used a halogen light source. The distance between the lamp and the device was set to match the short circuit current density value from RT *I–V* measurements under the solar simulator. All solar cell parameters gained from the fittings of temperature dependence measurements correspond to the total area of the device.

The temperature dependence of V_{OC} is often used to determine the dominant recombination processes in solar cells. It is known that at temperatures close to room temperature the V_{OC} (*T*) curve shows a linear part and the extrapolation of this line to 0 K results in the activation energy Φ [19–21]. In the case of $\Phi < E_g$, the dominant recombination is related to the interface recombination. However, in our case, the V_{OC} (*T*) curve shows only a limited number of points in the V_{OC} (*T*) curve, which show a linear trend. This is an indication that the activation energy $\Phi \approx 1.3$ eV is probably not completely correct.

In order to get additional information about solar cell properties we performed a fitting of all *I–V* curves. Dark curves were fitted using a double diode model:
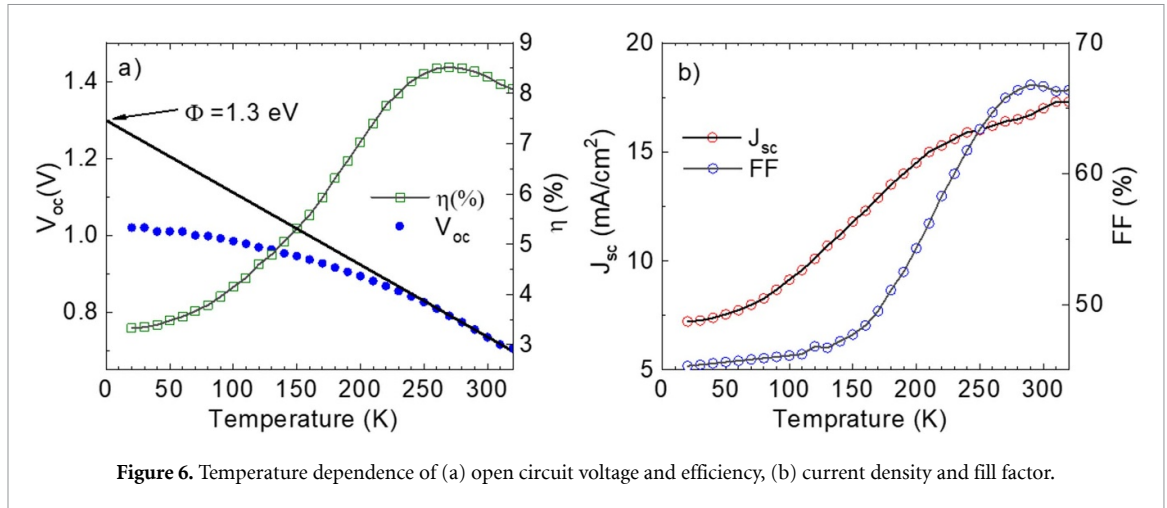
Figure 6. Temperature dependence of (a) open circuit voltage and efficiency, (b) current density and fill factor.

$$J = J_{01}\left\{\exp\left[\frac{q(V+JR_S)}{n_1 kT}\right] - 1\right\} + J_{02}\left\{\exp\left[\frac{q(V+JR_S)}{n_2 kT}\right] - 1\right\} + \frac{V+JR_S}{R_{SH}} \tag{1}$$

and illuminated curves were fitted using a single diode model:

$$J = J_0\left\{\exp\left[\frac{q(V+JR_S)}{nkT}\right] - 1\right\} + \frac{V+JR_S}{R_{SH}} - J_L \tag{2}$$

$$\text{where } J_0 = J_{00}\exp\left(\frac{-\Phi_B}{nkT}\right) \tag{3}$$

is the saturation and J_L the photogenerated current densities. The expression kT is the thermal energy where k is the Boltzmann constant and T the absolute temperature. The diode ideality factor n, series resistance R_S and parallel shunt resistance R_{SH} account for the non-ideal behavior of the solar cell. Here J_{00} is an only weakly temperature-dependent pre-factor, Φ_B is the activation energy of the saturation current. All the fittings were done using an algorithm proposed in [22] and ideality factors were not fixed during the fittings. An example of this fitting for $T = 300$ K and $T = 120$ K is given in figures 7(a)–(d).

The dark curves in figures 7(a) and (b) show typical non-ideal solar cell double diode behavior, where the first diode has so-called 'normal' behavior and the second diode has a very high value of ideality factor at different temperatures related to different recombination processes. At room temperature n_1 and n_2 have values 1.62 and 3.7, respectively. Such a high value of the ideality factor for the second diode represents a tunneling component, which has a similar exponential dependence to a diode. It is often called a 'weak' diode [23]. Therefore we do not present parameters for this diode and show only results for the first 'normal' diode.

The results of light curve fitting in figures 7(c) and (d) show that our cell has quite large current loss due to parallel shunt resistance R_{SH} at lower temperature ($T = 120$ K), while at room temperature due to the relatively high value of R_{SH} only diode current can be used in the fitting. At higher voltages, the role of series resistance R_S is also seen. Both resistances have a certain temperature dependence; see figures 8(a) and (b).

R_S shows a simple exponential dependence for both light and dark:

$$R_S(T) = R_{S0}/(1 + \beta \exp(-E_a/kT)) \tag{4}$$

with activation energies $E_a = 59$ meV and $E_a = 99$ meV for light and dark curves, respectively. In most cases this activation energy is assigned to the back contact barrier height. The difference between activation energies for the dark and light cases is an indication of a small photoconductivity. More complicated behavior can be observed for R_{SH} in dark and light; see figure 8(b). At higher temperatures, R_{SH}^{light} of the light curves increases almost linearly with temperature and therefore the current loss due to R_{SH}^{light} is smaller at higher temperatures. This ohmic behavior of R_{SH}^{light} can be related to ohmic shunts due to pinholes in the polymer layer between crystals or via low-resistance grain boundaries, because some monograins are formed from separate crystal blocks. At low temperatures, R_{SH}^{light} increases again, but this exponential increase has a different origin related to thermal activation of the semiconductor layer. It has an activation energy $E_a = 19.9 \pm 0.5$ meV. We assume that this rather small activation energy is related to some shallow trap level in the CdS buffer layer. However, the R_{SH}^{dark} values obtained from the dark curves are almost 1000 times higher than the values obtained for the light curves. While the decrease of R_{SH}^{light} with illumination is also observed in

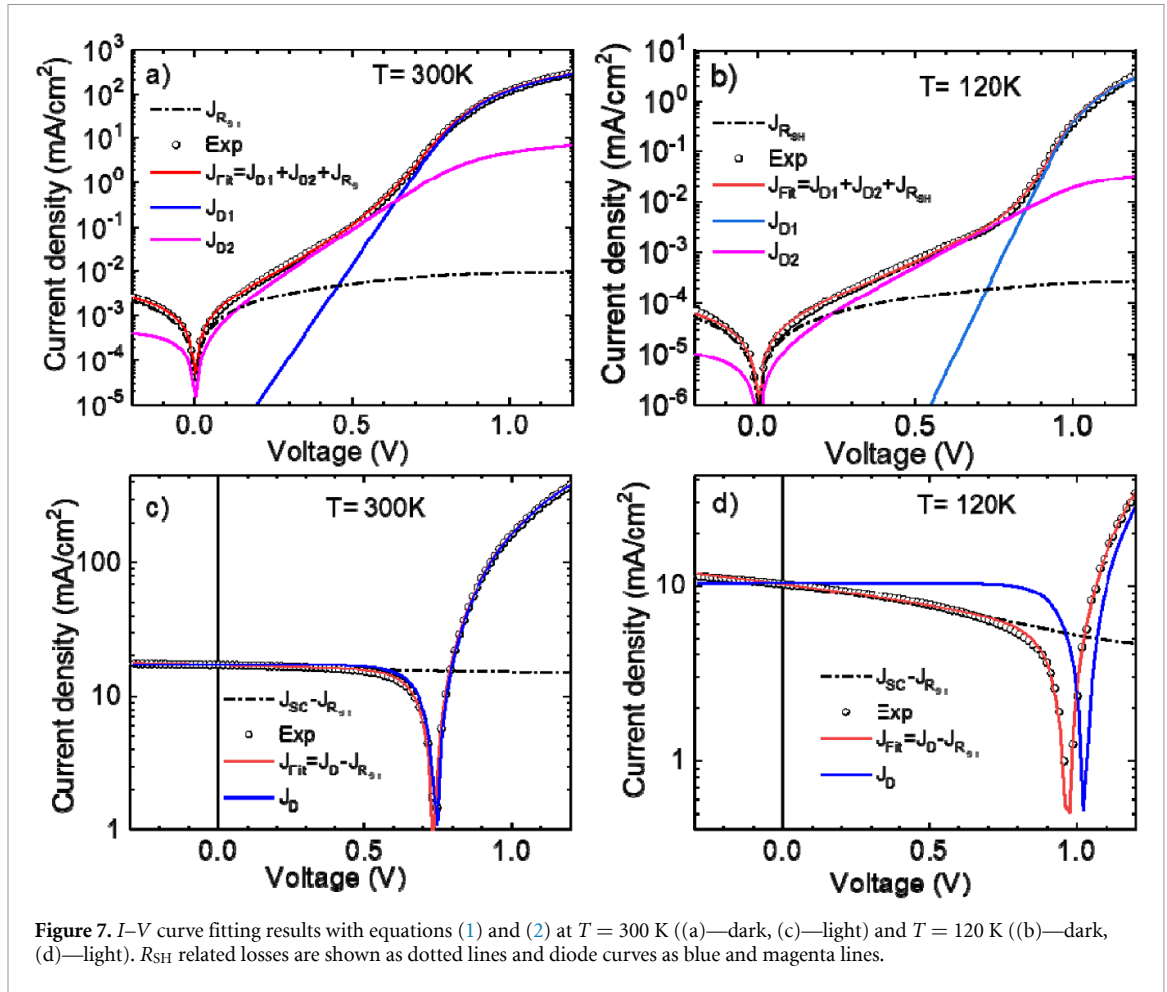**Figure 7.** I–V curve fitting results with equations (1) and (2) at $T = 300$ K ((a)—dark, (c)—light) and $T = 120$ K ((b)—dark, (d)—light). R_{SH} related losses are shown as dotted lines and diode curves as blue and magenta lines.
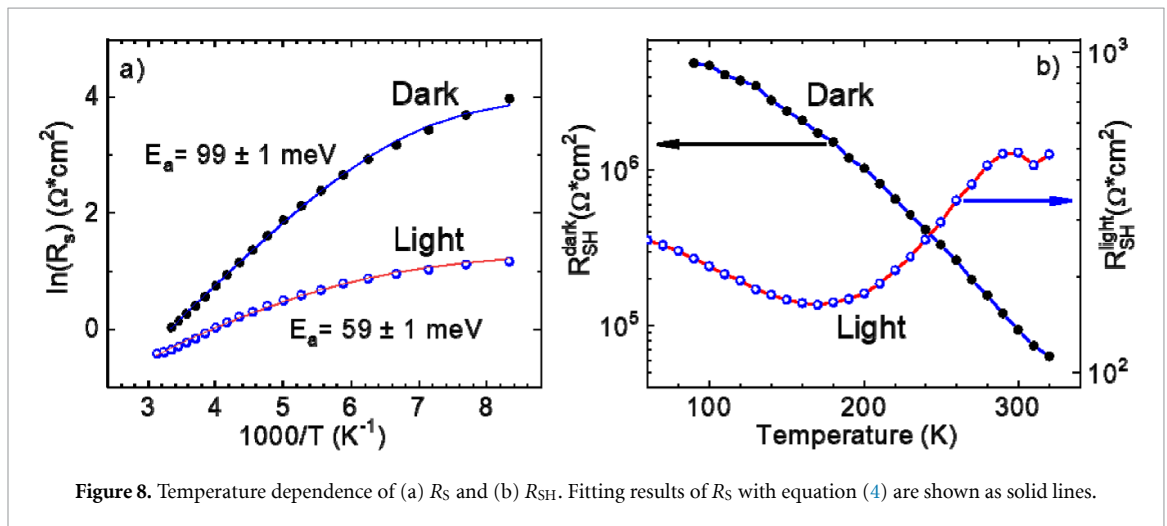

Figure 8. Temperature dependence of (a) R_S and (b) R_{SH}. Fitting results of R_S with equation (4) are shown as solid lines.

thin film solar cells [24], in our case the decrease is larger than expected. This means that the shunting current density is strongly influenced by the illumination and is probably related to the photoconductivity of the buffer layer. The CdS layer is around the crystals when the grains are embedded into the polymer layer. In the back contact formation process, it will be removed from the back side by etching and mechanical polishing, but a low probability remains that the CdS layer can be in touch with the back contact.

The temperature dependence of the diode ideality factor n usually gives valuable information about possible recombination mechanisms in solar cells [25]. In the case of tunneling-assisted interface recombination, it was shown that the temperature dependence of the ideality factor is given by [26]:

$$n = \frac{E_{00}}{\alpha kT}coth\left(\frac{E_{00}}{kT}\right),$$
(5)
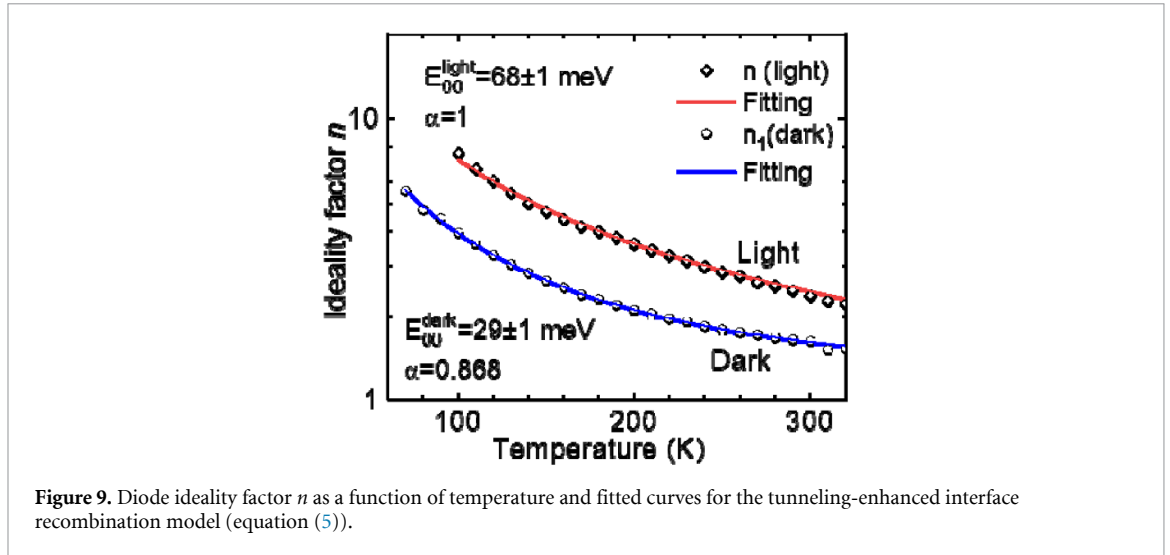
Figure 9. Diode ideality factor *n* as a function of temperature and fitted curves for the tunneling-enhanced interface recombination model (equation (5)).

where the characteristic tunneling energy E_{00} is a function of the net acceptor concentration N_A:

$$E_{00} = (q\hbar/2) \left[N_A/(m^*\varepsilon)\right]^{0.5}, \tag{6}$$

where $\hbar$—Planck constant, q—the elementary charge, ε—the semiconductor's dielectric constant, m^*—the effective tunneling mass, and

$$\alpha = \frac{\omega_p/\varepsilon_p}{\omega_p/\varepsilon_p + \omega_n/\varepsilon_n}, \tag{7}$$

where ω_p, ω_n and ε_p, ε_n are the space charge region widths and dielectric constants of the absorber and the buffer, respectively.

The temperature dependence of *n* and the fitting result with equation (5) are given in figure 9.

According to the fitting results, the dominant recombination in our solar cell is indeed related to tunneling-enhanced interface recombination with tunneling energy $E_{00} = 68$ meV. The same model is also true for dark curves, where the tunneling energy is $E_{00} = 29$ meV; however, the parameter α has a value of 0.868. This means that part of the space charge region extends into the buffer layer; see equation (7). The tunneling energy for light curves is slightly higher than the tunneling energy measured in thin film CZTSSe cells ($E_{00} = 41.5$ meV) [27] and is an indication that the carrier concentration in our CZTS is quite high; see equation (6). Therefore, the series resistance R_S of our cell is also fairly low, i.e. around 0.7 Ω cm^2 at room temperature.

More information can be obtained by examining the temperature dependence of saturation current density J_0. From equation (2) for J_0, the following expression can be derived:

$$\ln\left(\frac{J_0}{J_{00}}\right) = \frac{-\Phi_B}{nkT}. \tag{8}$$

By reorganizing equation (6), we obtain

$$n\ln(J_0) = n\ln(J_{00}) - \frac{\Phi_B}{kT}. \tag{9}$$

A plot of $n\ln(J_0)$ versus $1/kT$ should yield a straight line with a slope corresponding to the activation energy of the saturation current Φ_B; see figure 10.

The obtained activation energy values of the saturation current are lower than the estimated CZTS room temperature band gap energy $E_g = 1.548$ eV. It is known that values $\Phi_B < E_g$ would indicate interface recombination as the dominant mechanism due to Fermi-level pinning or band gap narrowing at the interface. It is interesting that the temperature dependence of V_{OC} provided lower activation energy $\Phi = 1.3$ eV; see figure 6(a). It is known that as soon as tunneling becomes important, the ideality factor *n* becomes temperature-dependent inducing nonlinear terms into V_{OC} vs T dependence and therefore, even for relatively high temperatures, the temperature dependence of V_{OC} may not give an accurate activation energy.
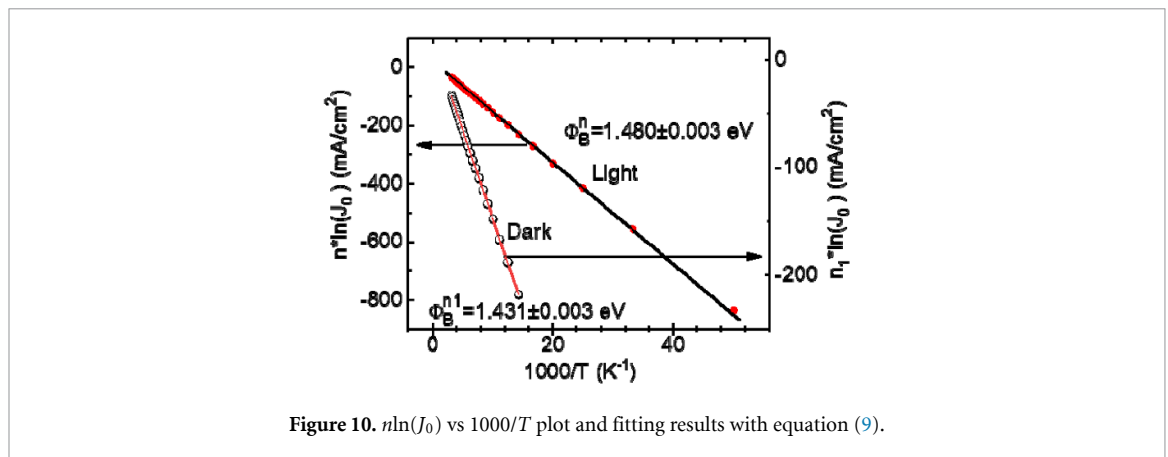
Figure 10. $n\ln(J_0)$ vs $1000/T$ plot and fitting results with equation (9).

4. Conclusions

The influence of Cd diffusion into the surface of CZTS and replacement of Cu-doped CdS by a fresh CdS buffer layer on the electrical behavior of the highest-efficiency CZTS monograin layer solar cell by temperature dependent I–V characteristics was analyzed. XPS surface analysis showed that after CZTS/CdS air-annealing an ultra-thin $Cu_2Zn_xCd_{1-x}SnS_4$ layer on CZTS crystals was formed. After replacing the annealed CdS:Cu with a fresh CdS buffer layer, device efficiency of 11.7% was achieved. The V_{OC} value improved slightly from 723 mV to 735 mV, but the main improvement was in the current density value from 20.5 to 23.6 mA cm^{-2}, and in FF from 59.4% to 67.7%. The serial resistance was significantly reduced from 2.4 Ω cm^2 to 0.67 Ω cm^2. To understand in more detail the electrical behavior of the highest-efficiency CZTS monograin layer solar cell, the temperature-dependent current–voltage characteristics were analyzed. According to the fitting results, the dominant recombination in our solar cell is related to tunneling-enhanced interface recombination with tunneling energy $E_{00} = 68$ meV. Analysis of the temperature dependence of R_{SH} indicated two types of shunts in our device, which remains a future challenge.

Data availability statement

The data that support the findings of this study are available upon reasonable request from the authors.

Acknowledgments

ORCID iDs

M Kauk-Kuusik ⬤ https://orcid.org/0000-0003-0071-8568
K Timmo ⬤ https://orcid.org/0000-0001-6054-6783
K Muska ⬤ https://orcid.org/0000-0002-8037-5675
M Pilvet ⬤ https://orcid.org/0000-0002-2060-3699
J Krustok ⬤ https://orcid.org/0000-0002-4671-2332
M Danilson ⬤ https://orcid.org/0000-0001-8105-6812
V Mikli ⬤ https://orcid.org/0000-0002-2406-3562
M Grossberg-Kuusk ⬤ https://orcid.org/0000-0003-3357-189X

References

[1] Hages C J, Redinger A, Levcenko S, Hempel H, Koeper M J, Agrawal R, Greiner D, Kaufmann C A and Unold T 2017 Identifying the real minority carrier lifetime in nonideal semiconductors: a case study of kesterite materials *Adv. Energy Mater.* **7** 1700167
[2] Yan C *et al* 2018 Cu$_2$ZnSnS$_4$ solar cells with over 10% power conversion efficiency enabled by heterojunction heat treatment *Nat. Energy* **3** 764–72
[3] Larsen J K *et al* 2019 Cadmium free Cu$_2$ZnSnS$_4$ solar cells with 9.7% efficiency *Adv. Energy Mater.* **9** 1900439
[4] Liu F, Yan C, Huang J, Sun K, Zhou F, Stride J A, Green M A and Hao X 2016 Nanoscale microstructure and chemistry of Cu$_2$ZnSnS$_4$/CdS interface in kesterite Cu$_2$ZnSnS$_4$ solar cells *Adv. Energy Mater.* **6** 1600706

[5] Su Z *et al* 2020 Device postannealing enabling over 12% efficient solution-processed Cu$_2$ZnSnS$_4$ solar cells with Cd^{2+} substitution *Adv. Mater.* **32** 2000121

[6] Kauk-Kuusik M, Timmo K, Muska K, Pilvet M, Krustok J, Josepson R, Brammertz G, Vermang B, Danilson M and Grossberg M 2021 Detailed insight into the CZTS/CdS interface modification by air annealing in monograin layer solar cells *ACS Appl. Energy Mater.* **4** 12374–82

[7] Visoly-Fisher I, Dobson K D, Nair J, Bezalel E, Hodes G and Cahen D 2003 Factors affecting the stability of CdTe/CdS solar cells deduced from stress tests at elevated temperature *Adv. Funct. Mater.* **13** 289–99

[8] Abou-Ras D, Kostorz G, Romeo A, Rudmann D and Tiwari A N 2005 Structural and chemical investigations of CBD- and PVD-CdS buffer layers and interfaces in Cu(In,Ga)Se$_2$-based thin film solar cells *Thin Solid Films* **480–481** 118–23

[9] Ben Messaoud K, Buffière M, Brammertz G, ElAnzeery H, Oueslati S, Hamon J, Kniknie B J, Meuris M, Amlouk M and Poortmans J 2015 Impact of the Cd^{2+} treatment on the electrical properties of Cu$_2$ZnSnSe$_4$ and Cu(In,Ga)Se$_2$ solar cells *Prog. Photovolt., Res. Appl.* **23** 1608–20

[10] Sun K, Yan C, Huang J, Sun K, Sun H, Jiang L, Deng X, Stride J, Hao X and Liu F 2018 Minority lifetime and efficiency improvement for CZTS solar cells via Cd ion soaking and post treatment *J. Alloys Compd.* **750** 328–32

[11] Nakada T and Kunioka A 1999 Direct evidence of Cd diffusion into Cu(In,Ga)Se$_2$ thin films during chemical-bath deposition process of CdS films *Appl. Phys. Lett.* **74** 2444–6

[12] Sun L, Wang W, Hao L, Jia Z, Zhao Y, Zhi G and Yao H 2022 Influence mechanism of Cd ion soaking on performance of flexible CZTSSe thin film solar cells *Mater. Sci. Semicond. Process.* **138** 106301

[13] Timmo K, Altosaar M, Pilvet M, Mikli V, Grossberg M, Danilson M, Raadik T, Josepson R, Krustok J and Kauk-Kuusik M 2019 The effect of Ag alloying of Cu$_2$(Zn,Cd)SnS$_4$ on the monograin powder properties and solar cell performance *J. Mater. Chem.* A **7** 24281–91

[14] Timmo K, Kauk-Kuusik M, Pilvet M, Raadik T, Altosaar M, Danilson M, Grossberg M, Raudoja J and Ernits K 2017 Influence of order–disorder in Cu$_2$ZnSnS$_4$ powders on the performance of monograin layer solar cells *Thin Solid Films* **633** 122–6

[15] Kauk-Kuusik M, Timmo K, Danilson M, Altosaar M, Grossberg M and Ernits K 2015 p–n junction improvements of Cu$_2$ZnSnS$_4$/CdS monograin layer solar cells *Appl. Surf. Sci.* **357** 795–8

[16] Ramasamy K, Zhang X, Bennett R D and Gupta A 2013 Synthesis, photoconductivity and self-assembly of wurtzite phase Cu$_2$Cd$_x$Zn$_{1-x}$SnS$_4$ nanorods *RSC Adv.* **3** 1186–93

[17] Xiao Z-Y *et al* 2013 Bandgap engineering of Cu$_2$Cd$_x$Zn$_{1-x}$SnS$_4$ alloy for photovoltaic applications: a complementary experimental and first-principles study *J. Appl. Phys.* **114** 183506

[18] Zhou R, Yu M, Tweddle D, Hamer P, Chen D, Hallam B, Ciesla A, Altermatt P P, Wilshaw P R and Bonilla R S 2020 Understanding and optimizing EBIC pn-junction characterization from modeling insights *J. Appl. Phys.* **127** 24502

[19] Rau U and Schock H-W 1999 Electronic properties of Cu(In,Ga)Se$_2$ heterojunction solar cells—recent achievements, current understanding, and future challenges *Appl. Phys.* A **69** 131–47

[20] Krustok J, Josepson R, Danilson M and Meissner D 2010 Temperature dependence of Cu$_2$ZnSn(Se$_x$S$_{1-x}$)$_4$ monograin solar cells *Sol. Energy* **84** 379–83

[21] Scheer R and Schock H-W 2011 *Thin Film Heterostructures* (Weinheim: Wiley-VCH Verlag GmbH & Co. KGaA)

[22] Suckow S, Pletzer T M and Kurz H 2014 Fast and reliable calculation of the two-diode model without simplifications *Prog. Photovolt., Res. Appl.* **22** 494–501

[23] Williams B L, Smit S, Kniknie B J, Bakker K J, Keuning W, Kessels W M M, Schropp R E I and Creatore M 2015 Identifying parasitic current pathways in CIGS solar cells by modelling dark *J–V* response *Prog. Photovolt., Res. Appl.* **23** 1516–25

[24] Mosavi A, Bertalan B, Imre F, Nadai L and Gorji N E 2020 Electrical characterization of CIGS thin-film solar cells by two- and four-wire probe technique *Mod. Phys. Lett.* B **34** 2050102

[25] Nadenau V, Rau U, Jasenek A and Schock H W 2000 Electronic properties of CuGaSe$_2$-based heterojunction solar cells. Part I. Transport analysis *J. Appl. Phys.* **87** 584–93

[26] Rau U, Jasenek A, Schock H, Engelhardt F and Meyer T 2000 Electronic loss mechanisms in chalcopyrite based heterojunction solar cells *Thin Solid Films* **361–362** 298–302

[27] Carter N J, Hages C J, Moore J E, McLeod S M, Miskin C K, Joglekar C, Lundstrom M S and Agrawal R 2013 Analysis of temperature-dependent current–voltage characteristics for CIGSSe and CZTSSe thin film solar cells from nanocrystal inks *2013 IEEE 39th Photovoltaic Specialists Conf. (PVSC)* (IEEE) pp 3062–5